## **CONDENSED MATTER PHYSICS**

# Accessing bands with extended quantum metric in kagome Cs<sub>2</sub>Ni<sub>3</sub>S<sub>4</sub> through soft chemical processing

Graciela Villalpando<sup>1</sup>\*, Milena Jovanovic<sup>1,2</sup>, Brianna Hoff<sup>1</sup>, Yi Jiang<sup>3</sup>, Ratnadwip Singha<sup>1,4</sup>, Fang Yuan<sup>1</sup>, Haoyu Hu<sup>3</sup>, Dumitru Călugăru<sup>5</sup>, Nitish Mathur<sup>1</sup>, Jason F. Khoury<sup>1,6</sup>, Stephanie Dulovic<sup>1</sup>, Birender Singh<sup>7</sup>, Vincent M. Plisson<sup>7</sup>, Connor J. Pollak<sup>1</sup>, Jaime M. Moya<sup>1</sup>, Kenneth S. Burch<sup>7</sup>, B. Andrei Bernevig<sup>3,5,8</sup>, Leslie M. Schoop<sup>1</sup>

Flat bands that do not merely arise from weak interactions can produce exotic physical properties, such as superconductivity or correlated many-body effects. The quantum metric can differentiate whether flat bands will result in correlated physics or are merely dangling bonds. A potential avenue for achieving correlated flat bands involves leveraging geometrical constraints within specific lattice structures, such as the kagome lattice; however, materials are often more complex. In these cases, quantum geometry becomes a powerful indicator of the nature of bands with small dispersions. We present a simple, soft-chemical processing route to access a flat band with an extended quantum metric below the Fermi level. By oxidizing Ni-kagome material Cs<sub>2</sub>Ni<sub>3</sub>S<sub>4</sub> to CsNi<sub>3</sub>S<sub>4</sub>, we see a two orders of magnitude drop in the room temperature resistance. However, CsNi<sub>3</sub>S<sub>4</sub> is still insulating, with no evidence of a phase transition. Using experimental data, density functional theory calculations, and symmetry analysis, our results suggest the emergence of a correlated insulating state of unknown origin.

Copyright © 2024 The Authors, some rights reserved; exclusive licensee American Association for the Advancement of Science. No claim to original U.S.
Government Works.
Distributed under a Creative Commons Attribution
NonCommercial
License 4.0 (CC BY-NC).

#### INTRODUCTION

Strongly correlated materials are highly sought after due to their corresponding assortment of electronic phenomena (1). Strong correlations can induce a wide range of desirable properties, including superconductivity, colossal magnetoresistance, and the fractional quantum Hall effect (1, 2). However, the ability to theoretically predict strongly correlated systems remains a challenge due to the many-body problem and the complex nature of electron-electron interactions (1, 3). Nonetheless, systems with a large density of states (DOS) and reduced kinetic energy naturally lead to correlated states. These possibilities are enriched in systems where flat bands emerge from the frustrated geometry of the lattice that also induces nontrivial band topology (1, 4-6). Flat bands have been shown to occur consistently in certain lattice structures with the correct orbitals that cancel hopping (4, 7). Therefore, one could design a strongly correlated system by identifying a lattice structure that contains the bands of interest near the Fermi level. One such system famous for its flat band physics is the kagome lattice (7-13). However, in real materials, the band structures are often different from the simple tightbinding models, and the correlated flat bands cannot be described by these simple models (4, 14). Recently, quantum geometry (15-18), which measures the spread of wavefunctions in bands, has gained more attention. It is a powerful tool to distinguish topological or obstructed (19, 20) flat bands from trivial atomic flat bands (21–23). Thus, a strategy to identify materials with correlated flat bands is to start with materials that crystallize in structures with frustrated lattices, such as the kagome lattice, and then compute the quantum metric for bands with small dispersion.

<sup>1</sup>Department of Chemistry, Princeton University, Princeton, NJ 08544, USA. <sup>2</sup>Department of Chemistry, North Carolina State University, Raleigh, NC 27606, USA. <sup>3</sup>Donostia International Physics Center (DIPC), Paseo Manuel de Lardizábal, 20018 San Sebastián, Spain. <sup>4</sup>Department of Physics, Indian Institute of Technology Guwahati, Assam 781039, India. <sup>5</sup>Department of Physics, Princeton University, Princeton, NJ 08544, USA. <sup>6</sup>School of Molecular Sciences, Arizona State University, Tempe, Arizona, 85287, United States. <sup>7</sup>Department of Physics, Boston College, Chestnut Hill, MA 02467, USA. <sup>8</sup>IKERBASQUE, Basque Foundation for Science, 48013 Bilbao, Spain. \*Corresponding author. Email: Ischoop@princeton.edu

The kagome lattice is trihexagonal, in which every hexagon contains a corner-sharing equilateral triangle. In tight-binding models, it famously gives rise to a flat band and two highly dispersed bands that cross at the K point of the Brillouin zone (BZ) for each atomic orbital present on the atoms composing the kagome lattice (10, 24).

However, despite the extensive number of compounds that contain kagome sublattices, most do not have bands stemming from the kagome lattice, or they are located very far away from the Fermi level, rendering these bands difficult for study or practical use (4). In addition, the kagome bands in real compounds usually do not appear only because of the kagome lattice but are better described by hybridization of bands from different atoms, as it was shown for FeGe (14), sometimes resulting in "accidental" flat bands, i.e., they are not a "kagome flat band", but they still have small dispersion and contain contributions from orbitals from the kagome layer and, importantly, can have a sizable quantum metric.

The simplest solution to accessing these bands would be to use metallic kagome compounds with flat bands lying near or at the Fermi level. Unfortunately, in many metallic kagome compounds, the presence of additional bands unrelated to the kagome system hinders accurate exploration of flat band physics (4, 10, 25, 26). FeSn and FeGe, for example, are metallic, two-dimensional (2D) kagome systems containing flat bands whose physics is muddled by other highly dispersive bands (10, 14, 27, 28). The convolution of bands has restricted scientists to using more complicated methods to study the physics of these flat bands, such as isolating the surface states from the bulk using tunneling spectroscopy (27). An alternative route for obtaining clean flat bands near the Fermi level in a bulk system is starting with an insulating kagome system and tuning the bands of interest to the Fermi level through methods such as doping (29-31). Doping studies of kagome compounds are not unheard of, with doping of metallic compounds through solid-state methods finding success in studying van Hove singularities (32). However, successful dopant-induced band tuning of insulating kagome systems to access flat bands has proven difficult.

One example of the challenge of doping Kagome systems is Herbertsmithite [M<sub>x</sub>ZnCu<sub>3</sub>(OH)<sub>6</sub>Cl<sub>2</sub>], a suspected ideal quantum spin liquid 2D kagome compound. This material was predicted to transition from a spin liquid to a strongly correlated Dirac metal upon successful electron doping  $M_xZn_{1-x}Cu_3(OH)_6Cl_2$  (30, 31, 33). If this compound could be electron-doped, various interesting properties could emerge, including f-wave superconductivity and ferromagnetism (30, 31). Unfortunately, recent studies on electron doping ZnLi<sub>x</sub>Cu<sub>3</sub>(OH)<sub>6</sub>Cl<sub>2</sub> using chemical methods to intercalate lithium were unable to experimentally produce these predicted properties. Instead, Kelly et al. (34) showed that electron doping the system did not increase metallicity and actually suppressed the magnetic features with increasing dopant concentration. In addition, the doped compound was found to be considerably more air-sensitive compared with its undoped counterpart. The insulating behavior of doped Herbertsmithite was later explained to result from added electrons being trapped in a polaronic state (35). This polaronic state is a consequence of the Cu<sup>2+</sup> hydroxide, and therefore, a different kagome host material would be needed to take advantage of electron doping as a viable route for Fermi level tuning. This study introduces Cs<sub>2</sub>Ni<sub>3</sub>S<sub>4</sub> as an alternative host material and a straightforward chemical doping method for band tuning. We present experimental data and density functional theory (DFT) calculations to support the promise of manipulating flat bands.

 $Cs_2Ni_3S_4$  has been reported in two crystallographic forms, a hexagonal one with a perfect kagome lattice and an orthorhombic one with a slightly distorted kagome lattice (see the "Reported crystal structures of  $Cs_2Ni_3S_4$ " section and fig. S1 in the Supplementary Materials) (36). As our synthesis repeatedly resulted in the latter, we focus here on this form, which crystallizes in space group *Fmmm*.  $Cs_2Ni_3S_4$  is a layered, orthorhombic crystal containing 2D, slightly distorted, kagome lattices of nickel lying in the *ab* plane (Fig. 1, A and B). The slight distortion in the kagome lattice is a product of the corner-sharing triangles of nickel being isosceles

rather than equilateral, with every triangle containing two sides with lengths of 2.913 Å and one side with a length of 2.963 Å (Fig. 1B). S-Ni-S layers are repeatedly stacked along the *c* axis, where cesium atoms reside in the interlayer gallery (Fig. 1A). Within the S-Ni-S layers, the nickels are square-planar coordinated by the sulfur atoms, with Ni—S bond distances of 2.212 and 2.219 Å (Fig. 1C).

To date, there are no reports of the electronic properties of Cs<sub>2</sub>Ni<sub>3</sub>S<sub>4</sub> (37). To test whether Cs<sub>2</sub>Ni<sub>3</sub>S<sub>4</sub> is a promising material to access flat bands, we performed generalized gradient approximation (GGA) Perdew-Burke-Ernzerhof (PBE) DFT calculations, which predict Cs<sub>2</sub>Ni<sub>3</sub>S<sub>4</sub> to be a semiconductor with a bandgap of 0.55 eV. (37) Furthermore, it contains bands with very small dispersion just below the Fermi level, which appear in both the hexagonal and orthorhombic structure (Fig. 1, D and E). The origin of those flat bands will be discussed later in this paper; we just note here that those are not the typical "kagome flat band", but they are band with low dispersion involving orbitals from the kagome lattice. As we will show later, they also exhibit an extended quantum metric. As DFT calculations predict the presence of a bandgap and considering the formal oxidation state of +2 (d8) for the square-planar coordinated Ni in Cs<sub>2</sub>Ni<sub>3</sub>S<sub>4</sub>, a nonmagnetic insulating ground state is anticipated a prediction also corroborated by DFT results. Because of the proximity of flat bands to the Fermi level, hole doping or oxidizing the compound might access correlated states. Furthermore, oxidation can potentially introduce magnetic moments on the Ni atoms. The possibility of accessing correlated states and the potential for changing magnetic properties make Cs<sub>2</sub>Ni<sub>3</sub>S<sub>4</sub> an ideal candidate for Fermi-level tuning through hole doping.

In this paper, we turn to soft chemical processing to cleanly and simply adjust the Fermi level into the flat band region, thus optimizing the electronic and magnetic properties of Cs<sub>2</sub>Ni<sub>3</sub>S<sub>4</sub>. To the best of our knowledge, this is the first time the kagome compound CsNi<sub>3</sub>S<sub>4</sub> has been achieved. Soft-chemical processing, in general, uses gentle chemical methods to remove or intercalate atoms into a

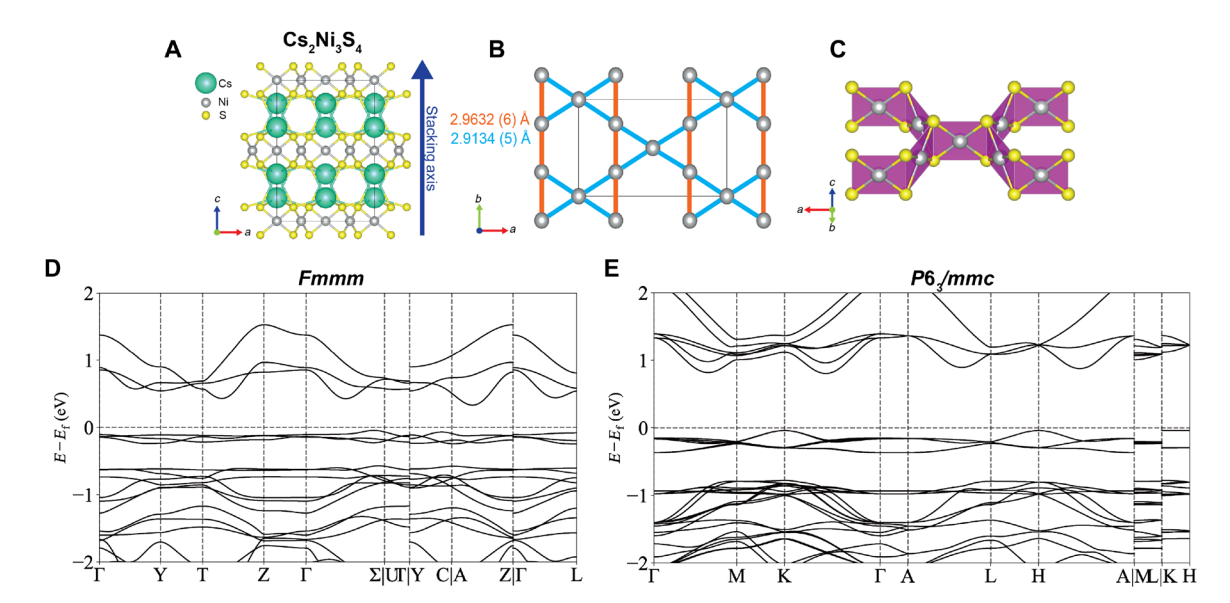


Fig. 1. Structure models for  $Cs_2Ni_3S_4$  from experimental powder x-ray diffraction refinements and calculated band structure. The stacking direction of the nickel layers sandwiched between double layers of cesium can be seen in (**A**) along with the stacking direction along the *c* axis. The slightly distorted kagome lattice is depicted in (**B**) with color-coded bond lengths. The square-planar Ni-S coordination environment is shown in (**C**). The *Fmmm* (**D**) and  $P6_3/mmc$  (**E**) band structure show the flat bands close to the Fermi level.

crystal structure and is a highly tunable method commonly used for 2D materials synthesis or as an alternative route for obtaining various phases (38-43). This study uses 0.1 M HCl in water to remove half the cesium atoms of the distorted-kagome compound Cs2Ni3S4 to produce CsNi<sub>3</sub>S<sub>4</sub>, oxidizing the compound, as shown in Fig. 2A. As a result, formally, one-third of the nickel atoms are oxidized to Ni<sup>3+</sup> (nickel d<sup>7</sup>), while the remaining two-thirds of the nickel retain a Ni<sup>2+</sup> oxidation state (nickel d<sup>8</sup>) (Fig. 2F). However, the holes might also be evenly distributed between the three Ni atoms. We find here that CsNi<sub>3</sub>S<sub>4</sub> exhibits an increase in magnetic moment, a two order of magnitude decrease in resistivity at room temperature and a notable increase in the Sommerfeld parameter of the specific heat. However, CsNi<sub>3</sub>S<sub>4</sub> still exhibits insulating behavior at low temperatures, as the resistivity sharply shoots up below 68 K. DFT calculations in this study suggest that a magnetic order that breaks the mirror symmetries could induce an insulating phase. However, we find no evidence in our data for the broken mirror symmetry. Thus, different scenarios for the ground state are discussed. Our results suggest that by converting Cs<sub>2</sub>Ni<sub>3</sub>S<sub>4</sub> to CsNi<sub>3</sub>S<sub>4</sub>, the Fermi level moves to the flat bands, decreasing the room temperature resistivity and increasing the effective mass of the electrons. The observed stark reduction of resistivity (two orders of magnitude at room temperature) could indicate that the system introduced here is more suitable for introducing correlated metallic states as compared to the previously mentioned kagome compounds (34). On the basis of this study, soft-chemical processing could be highly useful for accessing the desired bands while leaving the lattice mostly unchanged.

#### **RESULTS**

## Origin of flat bands in Cs<sub>2</sub>Ni<sub>3</sub>S<sub>4</sub>

As indicated earlier, Cs<sub>2</sub>Ni<sub>3</sub>S<sub>4</sub>, in both the hexagonal and orthorhombic phases, contains bands just below the Fermi level with a very low bandwidth of 0.4 eV (see the "Band structure of the undoped phase" section in the Supplementary Materials for more information). This is comparable to the bandwidth of quasi-flat band in kagome materials including FeGe, which is about 0.5 eV (14). As shown in fig. S2, those bands are mostly composed of Ni  $d_{xy}$  and  $p_x/p_y$  orbitals, as well as small contributions from Ni  $d_{x-y}^{2}$ and Ni d<sub>z</sub><sup>2</sup>. Thus, they are derived from the Ni-kagome lattice, but similarly to other kagome materials, bands from other atoms (here S) also contribute (14). To understand the origin of the flat bands and if they can be attributed to the kagome lattice, we constructed a tight binding model (details in the "Tight-binding model for the quasi-flat bands near Fermi level" section and fig. S4 in the Supplementary Materials). If we treat only the Ni  $d_{xy}$ orbitals in the model, we obtain the typical kagome band structure, with a total bandwidth of 1.3 eV, which contains both the kagome flat band and the two dispersed bands that cross at the K point [please see the Supplementary Materials for details on the model and choice of a local coordinate system on kagome sites, which explains why dxy orbitals alone can form kagome bands; for global coordinates, this is only possible for d<sup>2</sup> orbitals if only one d orbital is used (28)]. If we add hopping with S  $p_x/p_y$  orbitals as a perturbation, the bandwidth of the total kagome-derived band manifold is notably reduced to 0.3 eV. The "kagome flat band"

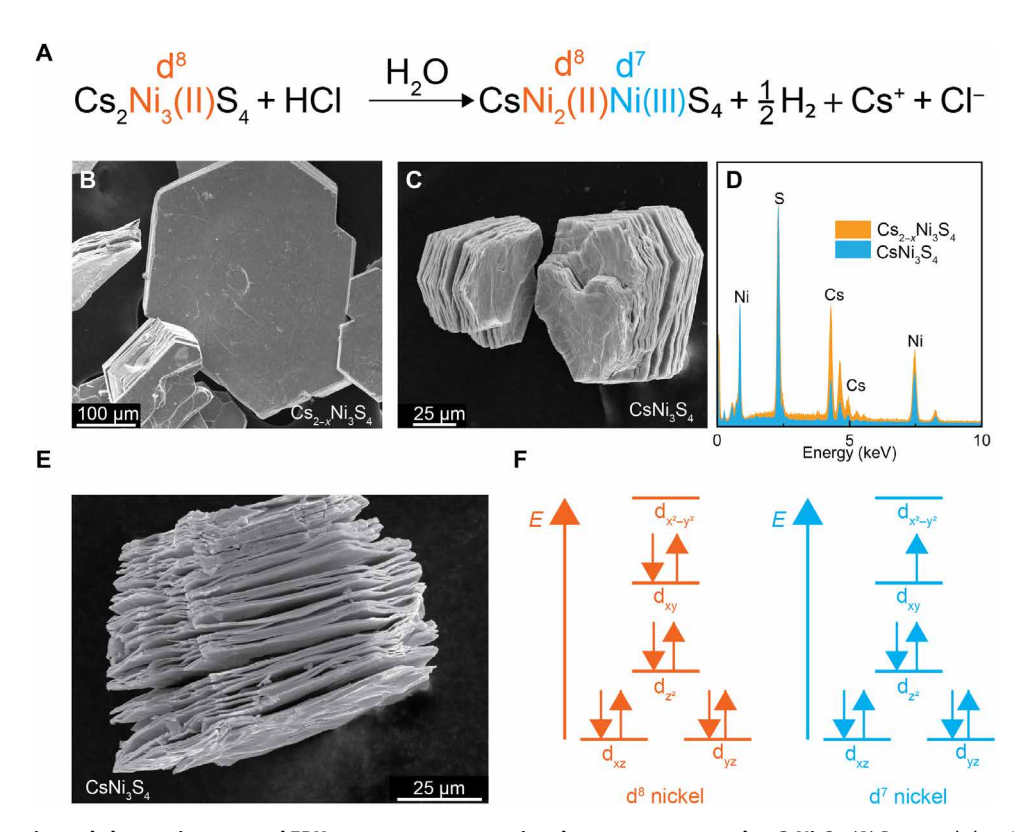


Fig. 2. Reaction schematics and electron images, and EDX spectroscopy comparing the parent compound to  $CsNi_3S_4$ . (A) Proposed chemical reaction for the synthesis of  $CsNi_3S_4$  with the  $d^7$  Ni(III) and  $d^8$  Ni(III) labeled within the chemical formula. Scanning electron microscope images of (B)  $Cs_{2-x}Ni_3S_4$  and (C)  $CsNi_3S_4$ . A decrease in cesium content is seen in the (D) EDX spectroscopy comparison. Additional electron microscope image of  $CsNi_3S_4$  emphasizing the delamination of the layers is shown in (E). Panel (F) contains the square-planar molecular orbital diagram for a  $d^7$  and a  $d^8$  nickel based on the decrease in cesium shown in (D).

now has a bandwidth of roughly 0.1 eV and lies on top of the manifold. As the dispersion of the entire manifold is small and comparable to that of other flat bands in the literature, we now refer to this entire structure as the flat bands. Thus, the flat bands originate from molecular orbitals formed between Ni d and sulfur p electrons, which bond with small dispersion within the kagome layer. To evaluate the potential of the flat band for correlations, we calculated the 2D Fubini study quantum metric for the six quasiflat bands (see the "Quantum geometry of the quasi-flat bands" section and fig. S5 in the Supplementary Materials), where we find that those bands are formed by molecular orbitals with a large spread and extended quantum metric. Hence, those bands are relevant for correlated flat band physics. While not equivalent to the typical kagome flat band, those bands are not atomically localized, and correlated physics is possible if it can be accessed via doping. We thus grew single crystals of Cs<sub>2</sub>Ni<sub>3</sub>S<sub>4</sub> and tried to access the flat bands through doping via Cs deintercalation.

#### Sample preparation

Bulk Cs<sub>2</sub>Ni<sub>3</sub>S<sub>4</sub> crystals were grown using a modified version of the method reported by Bronger et al. (36) with Cs<sub>2</sub>CO<sub>3</sub>, Ni, and S as the starting materials. The Cs<sub>2</sub>Ni<sub>3</sub>S<sub>4</sub> crystals are washed with water and ethanol. As discussed below, the parent compound most likely contains Cs defects, so we refer to the synthesized parent crystals from now on as Cs<sub>2-x</sub>Ni<sub>3</sub>S<sub>4</sub>, where x should be small. Crystals are flat, golden in color, and multidomain, where a single crystallite appears hexagonal-shaped. If left in air, the crystals quickly turn silver in color. If exposed to air for over 24 hours, then the parent compound will show the same powder x-ray diffraction (PXRD) pattern as acid-treated CsNi<sub>3</sub>S<sub>4</sub>; however, the energy-dispersive xray (EDX) spectroscopy analysis will have a much higher oxygen content and varying compositions. Therefore, Cs<sub>2-x</sub>Ni<sub>3</sub>S<sub>4</sub> crystals are stored in a glovebox. CsNi<sub>3</sub>S<sub>4</sub> was synthesized through soft chemical processing methods using 0.1 M HCl solution in air. Gas chromatography (GC) taken during the acid treatment process (fig. S6) shows the production of H<sub>2</sub> gas, which is also seen by bubbles forming on the surface of the crystals. The formation of H<sub>2</sub> gas during the acid treatment implies that the sample is being oxidized. A lack of any evidence of H-S stretching modes in the Raman spectroscopy measurements (fig. S7) also implies that the samples are oxidized during acid treatment and rules out a simple proton exchange reaction that would maintain the Ni oxidation state. X-ray photoelectron spectroscopy (XPS) was performed on both the parent and the acid-treated compound. The acidtreated compound shows an additional peak at 855.32 eV (fig. S8), in addition to the original peaks below 854 eV found in both the parent and acid-treated compound. The ratios between the peaks located at 855.32 and 851.30 eV are approximately 1:2, as expected. This additional peak and the ratios are indicative of a change in the oxidation state of some of the Ni(II) to Ni(III), further supporting the idea that only a third of the nickel is oxidized. The resulting crystals appear silver in color, aremore brittle, and airstable. CsNi<sub>3</sub>S<sub>4</sub> can also be easily exfoliated with tape (e.g., see fig. S9). Nonetheless, we were unable to exfoliate CsNi<sub>3</sub>S<sub>4</sub> down to the 2D level using the scotch tape method. Still, this makes CsNi<sub>3</sub>S<sub>4</sub> a great candidate for chemical exfoliation studies and shows that it can be cleaved easily. A detailed description of the synthesis details for both Cs2-xNi3S4 and CsNi3S4 can be found in the Materials and Methods.

#### Sample characterization

Scanning electron microscopy (SEM) images of  $Cs_{2-x}Ni_3S_4$  show hexagonal, layered platelets, as depicted in Fig. 2B. EDX gives an approximate 2:3:4 molar ratio of Cs:Ni:S (Fig. 2D). After acid treatment, samples still consist of hexagonal, layered platelets; however, the layers appear to be more delaminated compared with those of the untreated samples (Fig. 2, C and E). The increase in flakiness might contribute to their ability to be exfoliated, as described above. EDX analysis also shows a decrease of cesium in the system by approximately 50%, with a molar ratio of 1:3:4 of Cs:Ni:S (Fig. 2D). In addition, temperature and polarization-dependent Raman were performed to examine the crystal symmetry and look for structural phase transitions.

In addition to SEM/EDX/Raman spectroscopy, the acid-treated samples were examined using a high-resolution scanning transmission electron microscope (HRSTEM) (Fig. 3). The cross-section HRSTEM images (zone [100]) show a single layer of cesium atoms between layers of Ni. If imaged along the same zone, then the parent compound would display two cesium atoms (as shown in Fig. 1A) between the Ni-S layers. Acid treatment thus removed half of the cesium atoms (in agreement with EDX), and the remaining cesium moved to the center of the interlayer gap. Consequentially, the measured interlayer Ni-Ni distance from the HRSTEM image decreases from ~7.253 to ~6.75 Å, decreasing the unit cell length from 14.506 to 13.51 Å, as shown in Fig. 3A. Although most of the sample appears regular, as shown in Fig. 2A, there are areas where the Cs atoms appear elongated within the interlayer space, indicating some disorder in the Cs position (see fig. \$10). In addition, some areas still contain the parent compound, as evidenced by two layers of cesium, as shown in Fig. 3B. In this image, a defect is highlighted between the two phases, where the change in interlayer distance also becomes evident. This further shows that there are probably no intermediate Cs<sub>2</sub>Ni<sub>3</sub>S<sub>4</sub> phases; instead, the energy is likely minimized by expelling an entire cesium per formula unit (f.u.). Combined with our observation that CsNi<sub>3</sub>S<sub>4</sub> is not airsensitive in contrast to its parent, one can conclude that this soft chemically accessed phase is stable.

PXRD of the parent  $Cs_{2-x}Ni_3S_4$  (Fig. 4A) matches that of previously synthesized *Fmmm*  $Cs_2Ni_3S_4$ , as confirmed with Rietveld refinement (details of the refinement can be found in the "Solving the Structure of  $CsNi_3S_4$ " section in the Supplementary Materials). The

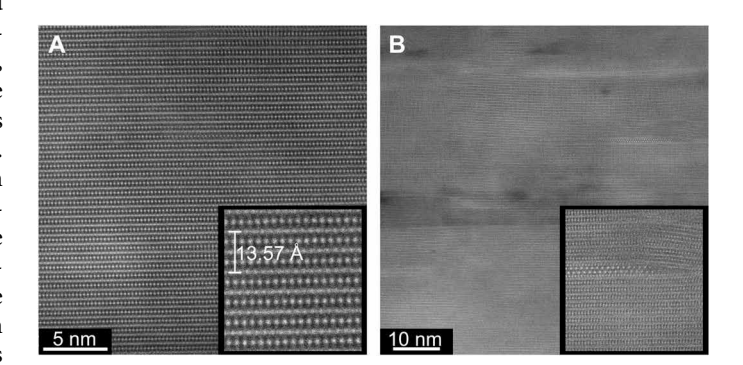


Fig. 3. HRSTEM images of  $CsNi_3S_4$  viewed along the ac plane (zone [100]). The inset of (A) shows the distance between three layers of Ni. The inset of (B) shows a defect within the crystal containing the double layer of cesium, which "zippers" into a single layer.

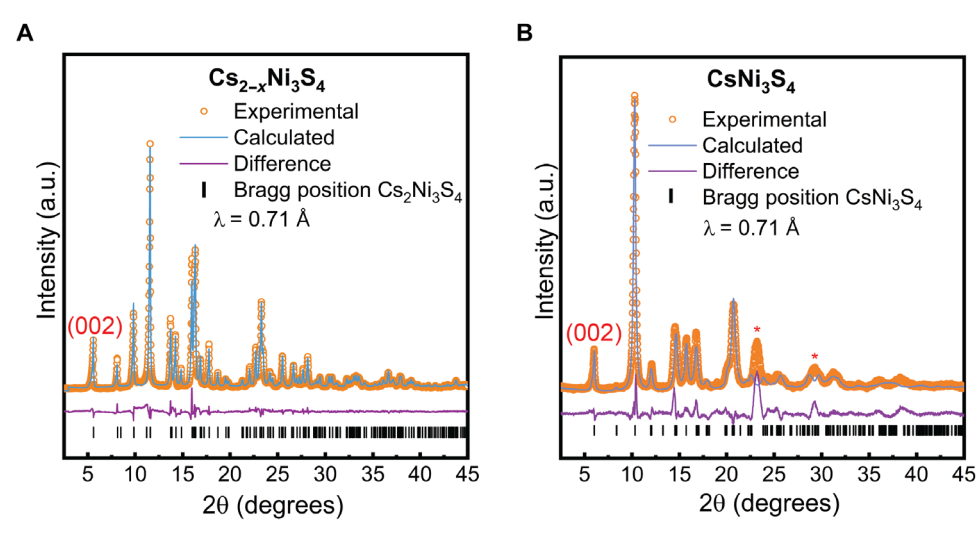


Fig. 4. PXRD of Cs<sub>2-x</sub>Ni<sub>3</sub>S<sub>4</sub> and CsNi<sub>3</sub>S<sub>4</sub>. (A) Cs<sub>2-x</sub>Ni<sub>3</sub>S<sub>4</sub> and (B) CsNi<sub>3</sub>S<sub>4</sub> with Rietveld calculated pattern, differences between the experimental and calculated, and Bragg positions. Peaks unable to be fit in (B) are marked with a red asterisk. These peaks are most likely due to cesium defects in the system. The (002) stacking peak is indicated in red for both (A) and (B).

PXRD pattern of CsNi<sub>3</sub>S<sub>4</sub> is notably different, as shown in Fig. 4B, implying a structural change upon cesium removal. The shifting of the (002) stacking peak in the parent compound (Fig. 4A) and CsNi<sub>3</sub>S<sub>4</sub> (Fig. 4B) respectively from  $2\theta = 5.58^{\circ}$  to  $5.99^{\circ}$  marks a decrease in layer distance along the stacking axis from  $\sim$ 7.21 to  $\sim$ 6.71 Å in agreement with the distances measured in HRSTEM. Removing one Cs from the system will lower the space group from Fmmm to Fmm2; as otherwise, the Cs will be multiplied by symmetry to 2 per f.u. Another possibility would be to keep the system in space group Fmmm and occupy the Cs with only half an atom. Both versions can be fit to the data with Fmmm resulting in a slightly lower  $R_{WP}$ percent than Fmm2 (See tables S1 and S2 and fig. S11), but only the former can be modeled with DFT due to occupancy. However, we would like to emphasize that we believe the Fmmm space group to be the better candidate for the real material. Peaks labeled with a red asterisk in Fig. 3B could not be fit. These peaks are most likely a consequence of the Cs not being fully removed throughout the system, as shown in Fig. 2B (inset), as they appear at angles similar to peaks of the parent compound.

Because of the relatively low quality of the PXRD data, a structural model could only be obtained via a feedback loop between DFT-aided structural optimization and Rietveld refinement, in conjunction with the HRSTEM images and electron diffraction. HRSTEM, selected-area electron diffraction along the [011] zone (fig. S12), and PXRD combined provided unit cell parameters with high confidence, but it was difficult to meaningfully refine atomic positions. Therefore, the atomic positions were optimized using DFT within fixed unit cell coordinates. The optimized geometry was then plugged into the Rietveld refinement, where the Cs atoms were allowed to disorder based on the visible Cs disorder in HRSTEM images (fig. S10). The resulting fit is shown in Fig. 3B, and the final structure is shown in Fig. 4. Both the PXRD data and the selected-area electron diffraction analysis confirm the orthorhombic geometry, yielding very similar lattice parameters. This similarity provides strong confidence in the unit cell model. In the polarized and helicity-resolved Raman spectroscopy measurements (see figs. S13 and S14), the observed symmetry aligns more

closely with a hexagonal space group. However, considering the likelihood of crystal twinning in the plane and minor orthorhombic distortion, one can also argue for the orthorhombic space group based on the data. In addition, Raman spectroscopy data also point toward the hexagonal space group for the parent compound (fig. S13), where a high-quality Rietveld fit on PXRD data unambiguously confirms the orthorhombic space group. This means that the Raman spectroscopy data are sensitive to in-plane twinning in both samples. As selected-area electron diffraction provides a more local probe and agrees with the orthorhombic setting, the proposed structure seems most reasonable.

The structure is closely related to the parent. Despite the changes in cesium content, it appears that the nickel kagome layers are retained in  $CsNi_3S_4$ , although the distortion becomes more prominent. Because of the decrease in interlayer distance, the Cs—S bond distances become rather short, likely causing the observed disorder in the Cs position. We have tested several solutions to increase the Cs—S bond distances in the model, where one was to change the S coordination of Ni from square planar to distorted tetrahedral. While this change in coordination also provides good Rietveld fits, DFT calculations with this geometry will not converge. We thus concluded that the Ni likely remains square planar coordinated (which DFT will predict in optimizations as well) and that the Cs are disordered. The latter also agrees with observations in HRSTEM. To account for the shortening of the Cs—S bonds, the Ni—S bond lengths are altered to 2.376, 2.056, 2.221, and 2.056 Å.

The Cs disorder was not modeled to calculate the band structure of CsNi3S4, as DFT calculations require full occupancy of atomic positions. While Cs<sub>2</sub>Ni<sub>3</sub>S<sub>4</sub> has no unpaired electrons, CsNi<sub>3</sub>S<sub>4</sub> should have one unpaired electron per f.u. (i.e., one-third per Ni). We expect the unpaired electron to be either located on specific Ni atoms or distributed along the Ni-kagome lattice. Oxidizing sulfur rather than Ni would be another possibility but seems unlikely based on the magnetic measurements shown below. We ran spin-polarized calculations with three distinct starting magnetic configurations to study the magnetic properties of CsNi<sub>3</sub>S<sub>4</sub>. The magnetic configurations were calculated using the strongly constrained and

appropriately normed (SCAN) functional for increased accuracy (44). The first was the standard isotropic magnetic configuration. This magnetic configuration converged to a ferromagnetic state one (FM I). The majority of the single unpaired electron was distributed evenly among Ni atoms, resulting in ~0.3 μB average magnetic moment per Ni atom. The total magnetization of this configuration is 0.95 µB per f.u. The second magnetic configuration used Vienna ab-initio Simulation Package's (VASP's) noncollinear settings and started with a magnetic field directed perpendicular to the kagome plane. This resulted in all spins in Ni atoms on a single layer being aligned with the field while alternating between up/down in the neighboring layers. This configuration converged to an antiferromagnetic (AFM) state, which is  $\sim$ 0.0015 eV more stable than the FM I. Same as in the ferromagnetic case, the unpaired single electron per f.u. was almost evenly distributed among all three Ni atoms, with an average magnetic moment of  $\sim$ 0.3 µB per Ni atom. The total magnetization was zero. The third configuration resembled the second one but spins in all layers pointed in the same direction, leading to ferromagnetic state II (FM II). This configuration can be achieved only through VASP's noncollinear settings. While this approach gives well-converged results, the spin-up and spin-down states are not defined anymore. We can only say that there are unpaired electrons, all perpendicular to the kagome plane and pointing in the same direction. This ferromagnetic state is more stable than the AFM state, but only by  $\sim$ 0.0004 eV. Similarly to the previous cases, the average magnetic moment per Ni atom is  $\sim 0.3 \mu B$ , and the total magnetic moment is  $\sim 0.98 \mu B$ .

The band structures of a PM, the AFM, and FM II configurations (Fig. 5, D to H) show that a loss of a Cs atom shifts the Fermi level into the bands originating from the Ni-S kagome bonding. The oxidation strengthens the bonding within the kagome lattice, increasing the band dispersion around the Fermi level. Orbital contributions (fig. S15) show that the same orbitals that comprised the flat bands in the parent compounds are responsible for the bands at the Fermi level in the oxidized compound. Some bands remain flat but are no longer separated from the lower energy bands. The paramagnetic structure is metallic and features several Dirac crossings at the Fermi level, which are protected by mirror symmetry. A detailed symmetry analysis can be found in the "Band structure in the doped phase" section in the Supplementary Materials. Adding magnetism to the calculation does not gap the band structure. In the FM II configuration, the Fermi level cuts through a very flat spin-up band; in the AFM case, the doubling of the bands causes the band structure to be more complex, but it remains metallic. Adding a Hubbard U of 2 (figs. S16 and S17) and 4 eV (Fig. 5, F and H), respectively, separates the bands and creates some gaps in certain parts of the BZ. Nonetheless, the system remains metallic, as the symmetry-protected Dirac nodes remain at the Fermi level. Spin-orbital coupling (SOC) can induce a small bandgap as shown in fig. S17, but this gap is too small to explain the strongly insulating behavior discussed below. However, should the mirror symmetry that protects the Dirac nodes be broken, the bands could flatten out, and a sizable gap could appear. Because of the uncertainty in our structural model discussed above, this scenario is a possibility, although we do not see any evidence for this loss of symmetry in either the diffraction or the Raman data. In the following, we will discuss the measured physical properties in light of the DFT calculations.

## **Magnetic characterization**

The in-plane (field perpendicular to the stacking plane shown in Fig. 1A) and the out-of-plane (parallel to the stacking plane) magnetic measurements of Cs<sub>2-x</sub>Ni<sub>3</sub>S<sub>4</sub> crystals and powder CsNi<sub>3</sub>S<sub>4</sub> are shown in Fig. 6. Note that due to the small crystallite size of the samples, the field orientations may not be exact but still show general trends. For pure Cs<sub>2</sub>Ni<sub>3</sub>S<sub>4</sub> samples, a diamagnetic phase would be expected due to the square planar coordination of Ni(II). This expectation agrees with DFT, which predicts a nonmagnetic ground state. In contrast to this expectation, the susceptibility measurements (Fig. 6, A and C) of Cs2-xNi3S4 show two transitions, a sharp upturn at  $\sim$ 35 and 28 K along the ab plane and c axis, respectively, and a peak in the zero-field cooled (ZFC) data at  $\sim$ 6 K for both field orientations. The data do not follow the Curie-Weiss behavior, regardless of the orientation of the applied magnetic field. In general, the maximum susceptibility reached is small, 0.098 emu mol <sup>-1</sup> Oe <sup>-1</sup>, which suggests that this signal does not come from the sample bulk but rather from a small impurity. Similar behavior has been seen in related kagome compounds washed with water and ethanol (45). A more in depth study by Hondou et al. (46) showed that the magnetic properties of kagome compound Rb<sub>2</sub>Ni<sub>3</sub>S<sub>4</sub> were greatly affected by the time spent in water, which was hypothesized to be due to water intercalation or Rb/S defects. On the basis of our observation of Cs loss in the acid-treated sample, it is most likely that the washing step removes a small amount of Cs. Therefore, we postulate that a small amount of the sample already transitioned to the more stable CsNi<sub>3</sub>S<sub>4</sub> phase, which is why we refer to the parent material as  $Cs_{2-x}Ni_3S_4$ .

As a result of the small amount of CsNi<sub>3</sub>S<sub>4</sub> indicated in the magnetic measurements, we can use the data on the parent samples to understand the magnetic properties of CsNi<sub>3</sub>S<sub>4</sub>, as the untreated samples allow measurements with different field orientations, unlike the oxidized sample, in which crystals are so small that magnetic measurements could only be performed on a powder. If the field is aligned along the c axis (stacking direction), then the ZFC susceptibility curve drops more sharply, suggesting that the moments are antiferromagnetically aligned along the stacking direction, whereas it is possible that the spins within each layer are aligned ferromagnetically. However, as the FC susceptibility keeps increasing, a different interpretation could also be a ferromagnetic structure, where domain wall movement causes a drop in susceptibility in the ZFC curves. We also want to reiterate the small energy difference within the two possible magnetic ground states in DFT (0.002 eV). The moment versus field diagrams (Fig. 6, B and D) show an S-shape all the way to room temperature for both the in-plane and out-of-plane field orientations. Both contain a small amount of hysteresis in the moment versus field at low temperatures (Fig. 6, B and D, inset). The hysteresis closes roughly around the same temperature on warming as the peak appears in the ZFC state, providing more evidence for the FM (ferromagnetic) scenario with domain movement. The fact that some S-shape remains up to room temperature points to additional ferromagnetic impurities. Generally, the S-shape is much more pronounced if the field is applied along the ab plane, which points to the AFM scenario, with ferromagnetic coupling within the layers and AFM coupling along the stacking direction. Again, the maximum moment reached at 7 T is very small, which suggests that these observations apply to a small impurity of CsNi<sub>3</sub>S<sub>4</sub> within  $Cs_{2-x}Ni_3S_4$  samples.

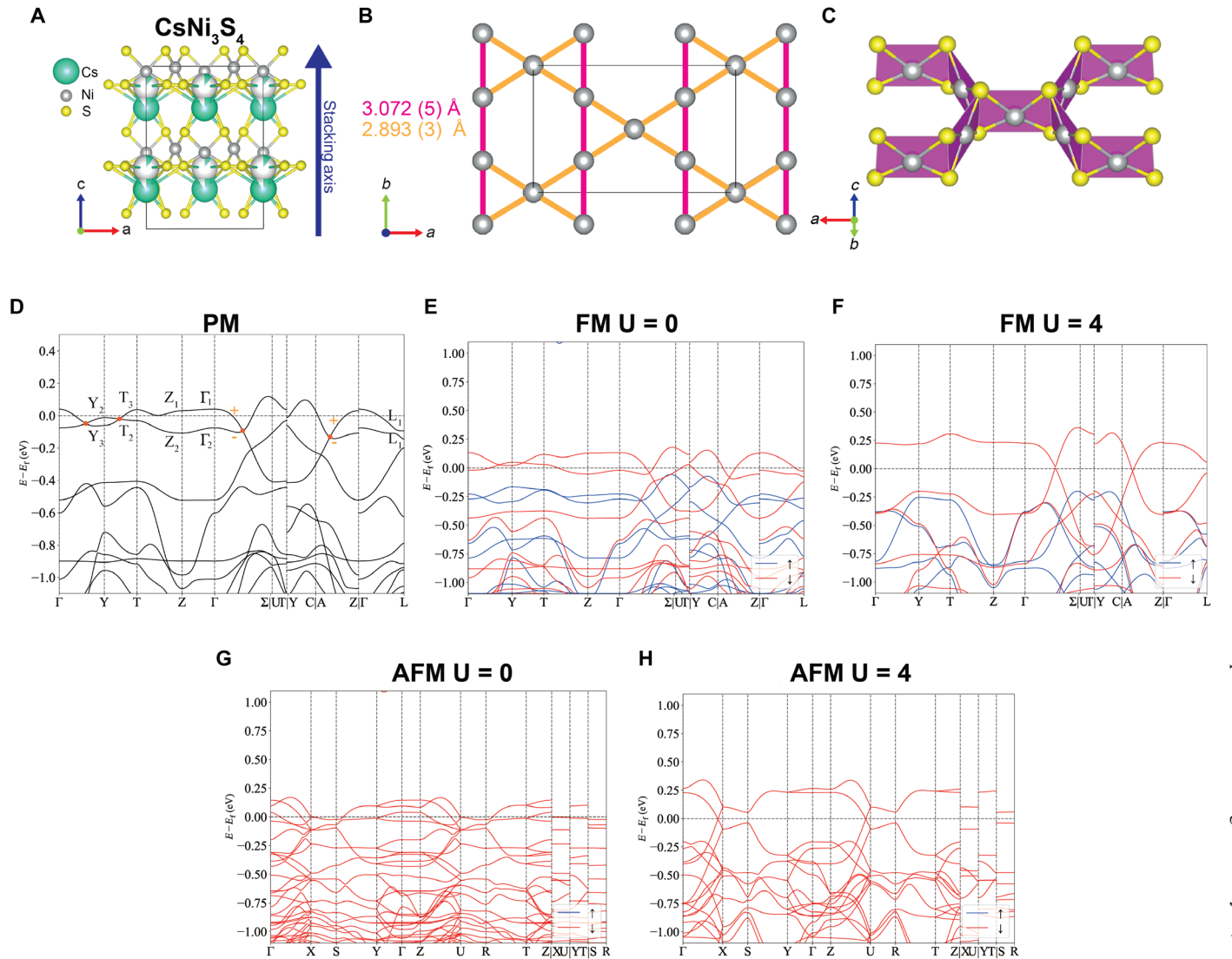


Fig. 5. Structure models for  $CsNi_3S_4$  from experimental PXRD refinements and calculated band structure. The stacking direction of the nickel layers sandwiched between single cesium layers can be seen in (**A**) along with the stacking direction along the *c* axis. On the basis of the results from the Rietveld refinement and HRSTEM, we included a small amount of Cs disorder in the structural models. The slightly distorted kagome lattice is depicted in (**B**) with color-coded bond lengths. The square-planar Ni-S coordination environment is shown in (**C**). The PM (paramagnetic), AFM, and FM II band structures (**D** to **H**) shows that the Fermi level resides in the flat bands. For the PM phase (D), irreproducible representations at high-symmetry points are marked, and the orange dots indicate Dirac crossings protected by mirror symmetry. Band structures for magnetic structures remain metallic, but adding a Hubbard U [(F) and (H)] widens the gap along most places of the BZ, unless at those points where mirror symmetry protects Dirac nodes.

The magnetic properties of  $CsNi_3S_4$  are similar, confirming the suspicion that small amounts of  $CsNi_3S_4$  cause the observations in  $Cs_{2-x}Ni_3S_4$  samples. Acid-treated  $CsNi_3S_4$  exhibits a magnetic transition at ~30 K and another at ~10 K (Fig. 6E). The moment versus field diagram also shows S-shaped curves below the transition temperature of 30 K, as well as wider hysteresis at 1.8 K (Fig. 5F, inset), which remains until 6.8 K. Here, the signature of the small ferromagnetic impurity is gone, indicating that it could have been dissolved during the acid treatment. Although the two compounds show similar character,  $CsNi_3S_4$  has a notably higher maximum susceptibility (~0.95 emu mol  $^{-1}Oe^{-1}$ ) and moment at 7 T (0.1701  $\mu_B$  per f.u.) compared to that of the undoped parent compound. However, this moment is still substantially

smaller than what is predicted by DFT for the FM case, which could point toward the AFM configuration (which also had a slightly lower ground state energy). Another possibility is that a field of 7 T is not enough to fully saturate the magnetic moment. Curie-Weiss fitting of the inverse susceptibility  $\chi^{-1}$ , where a small  $\chi_0$  that is subtracted produces an effective moment  $\mu_{\rm eff}$  of 1.354  $\mu_{\rm B}/f$ . u. (fig. S18), which is slightly smaller than the value Hund's rules predicts and what has previously been found for Ni³+ (~1.73) (45). However, this value is still close enough to the expected value for the proposed Ni oxidation mechanism. The slightly lower-than-expected value likely is a result of the observed impurities in PXRD and/or parent compound defects as seen in HRTEM (Fig. 3B, inset).

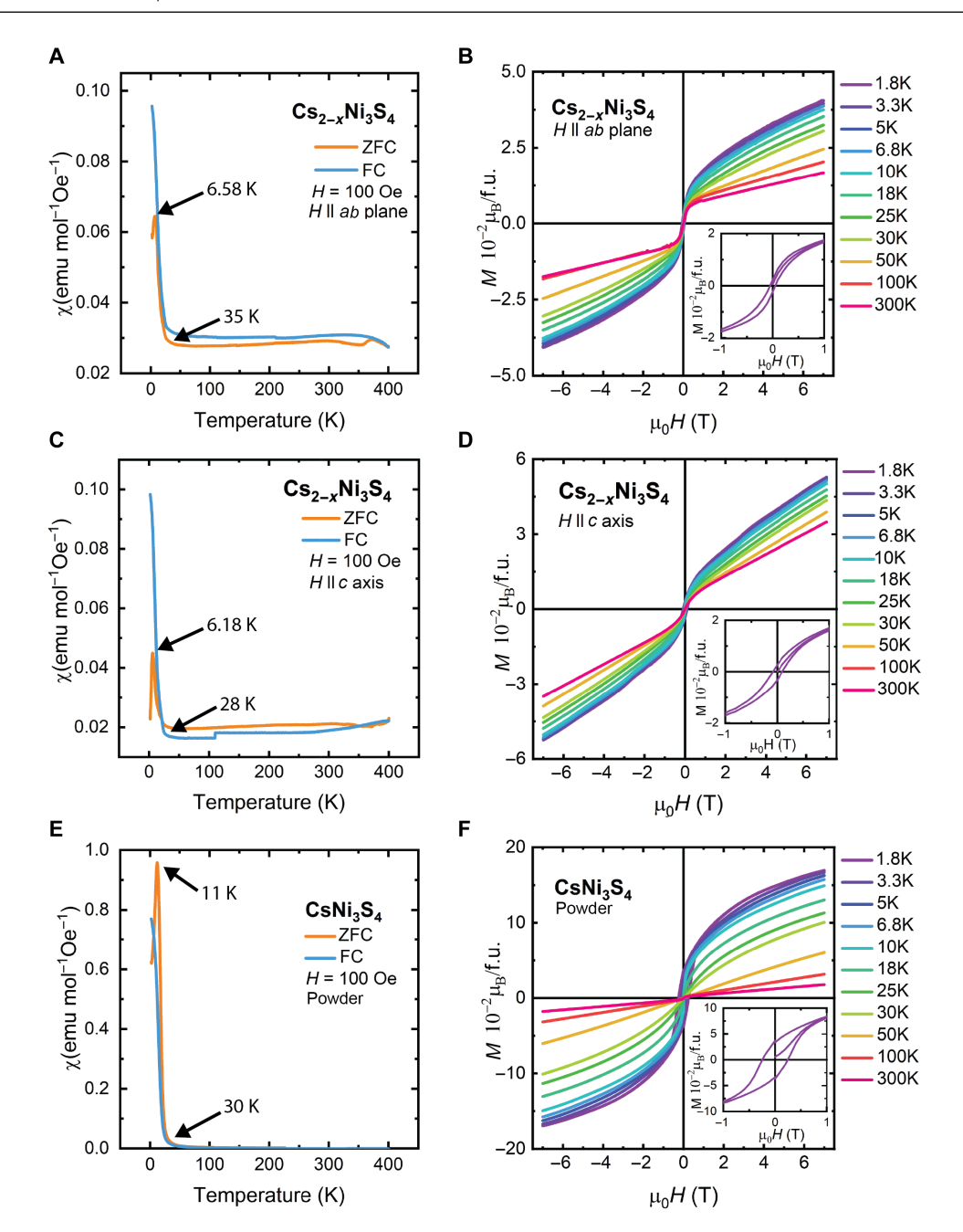


Fig. 6. Magnetometry measurements for Cs  $_{2-x}Ni_3S_4$  and CsNi $_3S_4$ . Magnetic characterization of both Cs  $_{2-x}Ni_3S_4$  (A to D) and CsNi $_3S_4$  (E and F). Cs  $_{2-x}Ni_3S_4$  has measurements along both the ab plane [(A) and (B)] and the c axis [(C) and (D)]. Insets shown in (B), (D), and (F) are taken at 1.8 K

The notable increase in magnetic moment from the bulk to the acid-treated sample is telling of the effect that cesium removal has on the electronic structure of the system. Removing half the cesium atoms would oxidize every third nickel in the kagome lattice, allowing unpaired electrons to contribute to the magnetic character seen in the acid-treated sample.

### **Electronic transport**

Devices for resistivity ( $\rho$ ) measurements were prepared from single crystals as described in Materials and Methods. The  $Cs_{2-x}Ni_3S_4$  crystal is insulating and exhibits a room-temperature resistivity of  $\sim$ 0.62 ohm·cm,

as shown in the inset of Fig. 7A with a notable increase in resistivity below  $\sim$ 72 K. Below 50 K, the resistivity became too high to measure accurately. If plotted as  $\ln(\rho)$ versus 1/T (fig. S19, A and B), then it becomes evident that the data do not follow the Arrhenius law, although it could be approximated with two different activation energies. These fits would yield a transport gap of 39 meV at higher temperatures (224 to 125 K) and 140.5 meV at low temperatures (fitting range of 69 to 55 K).

 $CsNi_3S_4$  samples show similar behavior (Fig. 7B); however, the high-temperature resistivity is two orders of magnitude lower compared to that of its untreated counterpart, with a resistivity of  $\sim$ 8.75 megohm cm at 300 K. We can relate the decrease in the

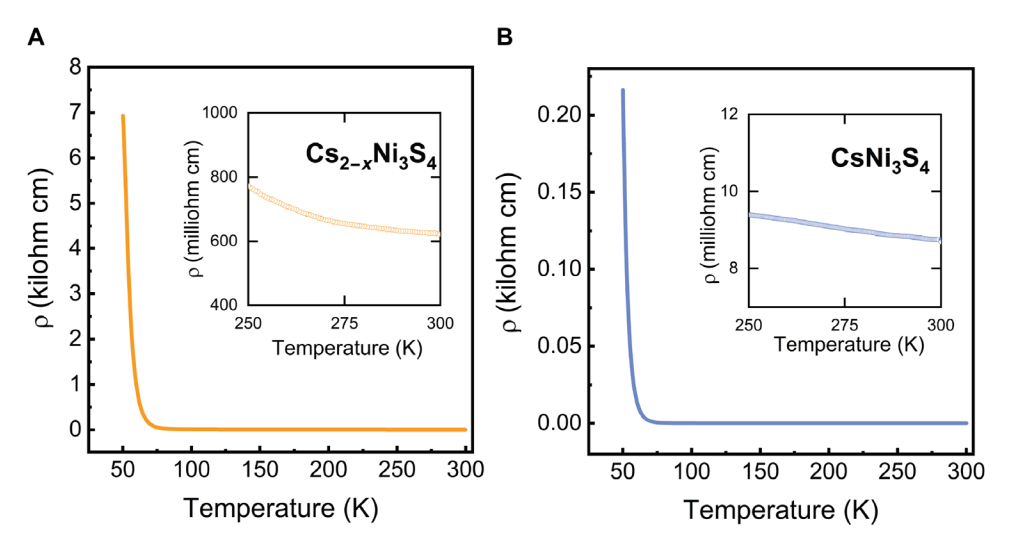


Fig. 7. Electronic transport measurements for  $Cs_{2-x}Ni_3S_4$  and  $CsNi_3S_4$ . Panels (A) and (B) show the resistivity measured for the parent compound and  $CsNi_3S_4$ , respectively, with insets emphasizing the two orders of magnitude difference in resistivity at high temperatures between both samples.

resistivity with the shift of the Fermi level to the valence bands, as predicted by DFT. Fitting  $ln(\rho)$  versus  $T^{-1}$  between 300 and 166 K with the Arrhenius equation yields an Arrhenius transport gap of ~18 meV, about half the gap of the parent compound (fig. S19C). Below ~60 K, the Arrhenius transport gap increases to 140 meV, which is similar to the value obtained by the parent. This is consistent with our previous findings suggesting that the parent compound contains small amounts of CsNi<sub>3</sub>S<sub>4</sub>, which are more conducting and thus dominate the low-temperature transport (fig. S19D). As shown in the Supplementary Materials, plotting the resistivity with a log scale reveals the two different regions of activation energy (fig. S20). The transport behavior of CsNi<sub>3</sub>S<sub>4</sub> changes very little with applied field (fig. S21), i.e., the effect of the field is negligible. In CsNi<sub>3</sub>S<sub>4</sub>, the temperature-induced change in the transport gap indicates a notable decrease in carriers. This is also visible in the sudden and very sharp increase in resistivity below ~68 K, which is approximately twice the magnetic transition temperature. Raman spectroscopy measurements at different temperatures see no change in the phonon spectrum and thus the symmetry of CsNi<sub>3</sub>S<sub>4</sub>, indicating that this is not a result of a structural phase transition. Preliminary Fourier transform infrared (FTIR) measurements (fig. S22) see a minimum reflectance that would correspond to a gap below approximately 0.5 eV, which agrees with the gap seen in the predicted band structure shown in Fig. 5 above the Fermi level. This gap size could also be consistent with the FM structure and a Hubbard U of 4 eV if mirror symmetry is broken in the crystal. It might be that the insulating behavior is related to a Mott gap opening slightly above the magnetic order. Usually Mott gaps are not related to the magnetic ordering temperature and appear at much higher temperatures. Another option would be a symmetry change around the transition temperature, which breaks mirror symmetry and breaks the Dirac nodes. However, this scenario is not consistent with our Raman studies. In general, the transport points to an insulating low-temperature ground state, which appears suddenly below ~68 K, whereas the sample is much less resistive above this temperature. The transport and Raman spectroscopy measurements on both compounds were repeated several times, and the results were consistent. In addition, transport measurements were repeated using sputtered gold contacts instead of directly contacting samples with silver paste, which also yielded consistent results.

#### Low-temperature heat capacity

Heat capacity samples were prepared as described in the Materials and Methods. Neither Cs 2-xNi<sub>3</sub>S<sub>4</sub> nor CsNi<sub>3</sub>S<sub>4</sub> pellets showed transitions (fig. S23) between 2 and 30 K, indicating that there are no changes at low temperatures in the free energy of the system. CsNi<sub>3</sub>S<sub>4</sub> was also measured to 250 K, as shown in fig. S24; however, no transitions were seen, which rules out structural changes as the origin of the sudden insulating behavior, consistent with the temperaturedependent Raman spectroscopy measurements (figs. S13 and S25). The low temperature–specific heat was fitted to Eq. 1, where  $C_p$  is the specific heat,  $\beta$  is the phonon contribution, and  $\gamma$  is the electron contribution, also known as the Sommerfeld coefficient. The Sommerfeld coefficient is, therefore, the y intercept for  $C_D/T$  versus  $T^2$ , as shown in Fig. 8. The fit yields a Sommerfeld coefficient of 14.49 and 43.99 mJ mol  $^{-1}$  K  $^{-2}$  for the parent compound and CsNi<sub>3</sub>S<sub>4</sub>, respectively. We checked if the larger Sommerfeld coefficient for CsNi<sub>3</sub>S<sub>4</sub> is repeatable (data of a second sample can be found in fig. S26) and found a similar value of 38 mJ mol <sup>-1</sup> K <sup>-2</sup>. The Sommerfeld parameter can be related to the DOS at  $\epsilon_f$ , as shown in Eq. 2. On the basis of that equation, we calculate the DOS at  $\varepsilon_f$  for the parent compound and CsNi<sub>3</sub>S<sub>4</sub> to be 6.32 and 18.67 eV <sup>-1</sup>f.u. <sup>-1</sup>, respectively. The meta-GGA DFT (SCAN) predicts a DOS of 0 eV <sup>-1</sup> f.u. <sup>-1</sup> for Cs<sub>2</sub>Ni<sub>3</sub>S<sub>4</sub> and  $4.345 \text{ eV}^{-1} \text{ f.u.}^{-1}$  for the AFM CsNi<sub>3</sub>S<sub>4</sub> phase (without *U*). In the FM I CsNi $_3$ S $_4$  phase, SCAN predicts 0.212 and 5.382 eV  $^{-1}$  f.u.  $^{-1}$  density of spin-up and spin-down states at the Fermi level, while for the FM II phase, the DOS is 4.335 eV  $^{-1}$  f.u.  $^{-1}$  (both times without U). In the case of the parent, the nonzero value can be attributed to the CsNi<sub>3</sub>S<sub>4</sub> phase. For the oxidized compound, the much lower value extracted by DFT as compared to the measurements indicates that the bands in the samples are flatter than predicted by DFT, again pointing toward correlations playing a role. It should be noted that Eqs. 1 and 2 were obtained through models based on monovalent metals that do not always translate to more complex systems; however, they are commonly used for complicated solid materials and give us some idea of the changes in electronic structure between both systems (48). The

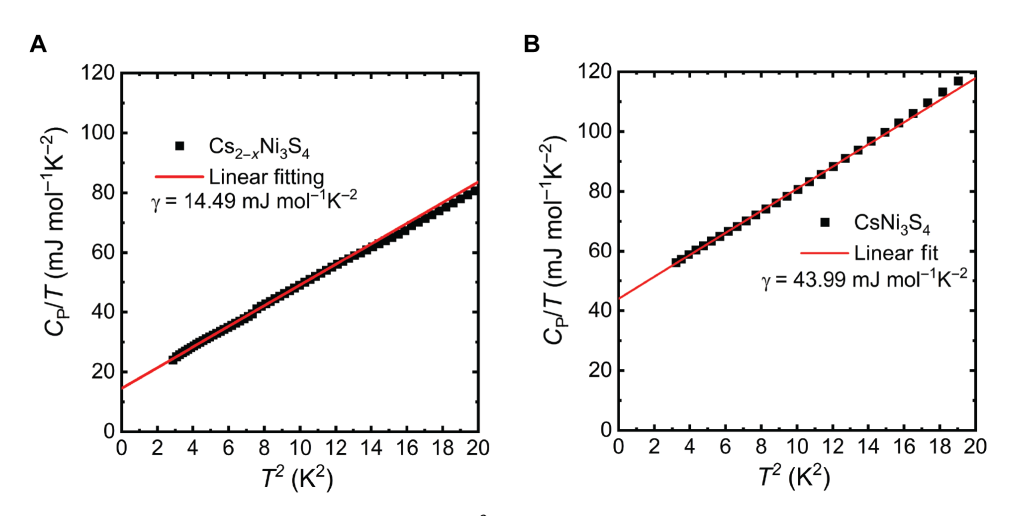


Fig. 8. Heat capacity measurements for Cs  $_{2-x}$ Ni $_3$ S $_4$  and CsNi $_3$ S $_4$ .  $C_p/T$  versus  $T^2$  of (A) Cs  $_{2-x}$ Ni $_3$ S $_4$  and (B) CsNi $_3$ S $_4$  with linear fittings.

notable increase in the Sommerfeld coefficient, along with the disparity between calculated and experimental values, has been seen in other kagome compounds with correlated metallic states. (49) The kagome compounds Ni<sub>3</sub>Sb and Ni<sub>3</sub>In show an over nine times increase in  $\gamma$  between the former and the latter, in addition to considerably larger values than theoretically expected (49). Ye *et al.* (49) attributed this to an energetic shift of the flat bands closer to the Fermi level. Together, our specific heat data support the idea of the presence of flat bands near the Fermi level. Further studies, such as scanning tunneling microscopy or angle-resolved photoemission spectroscopy, to visualize the band structure will help to understand this material better

$$\frac{C_{\rm p}}{T} = \beta T^2 + \gamma \tag{1}$$

$$N(\epsilon_{\rm f}) = \frac{3\gamma}{\pi^2 k_{\rm R}^2 N_{\rm A}}$$
 (2)

#### **DISCUSSION**

In summary, we successfully hole-doped the kagome compound Cs<sub>2</sub>Ni<sub>3</sub>S<sub>4</sub>, which has flat bands with extended quantum metric just below the Fermi level, by oxidatively removing one Cs per f.u. The reaction's oxidative nature was confirmed via hydrogen generation and the lack of S-H stretching modes in the Raman spectroscopy measurements. The structure of the first-time synthesized and airstable CsNi<sub>3</sub>S<sub>4</sub> was proposed via a combination of electron diffraction, PXRD, and DFT optimization. The predicted band structure of the previously unreported CsNi<sub>3</sub>S<sub>4</sub> compound is metallic, has the Fermi level cutting through bands with small dispersion, and predicts the unpaired electron on the Ni to magnetize. Adding a Hubbard U to the calculations can allow a bandgap to open when SOC is included, and the gap could be further enlarged when mirror symmetry is broken in the crystal. While magnetic order is experimentally observed, the moment does not saturate at 7 T. Still, the fluctuating Curie-Weiss moment is close to the expected value for one Ni<sup>3+</sup> per f.u., confirming that most of the oxidation appears on Ni rather than S. Upon oxidation, the room-temperature resistivity is also lowered considerably. Nonetheless, below ~68 K, CsNi<sub>3</sub>S<sub>4</sub> reveals the sudden onset of a highly insulating state.

While the insulating state might be fittingly described as induced by magnetic order, not all characteristics may agree with this picture, as it occurs without any clear change in the lattice structure. Furthermore, the specific heat provides no evidence of a phase transition but does reveal a large increase in the Sommerfeld coefficient. The specific heat and relatively small magnetic moment at 7 T could indicate the Kondo effect, which is caused by the scattering of conduction electrons due to magnetic impurities. However, these states are quite rare in d-electron systems, and one would expect a strong magnetic field effect on the resistivity and metallic transport at high temperatures (50-52). Anderson localization due to disorder in the system could also play a role in the occurrence of the insulating state. Although our system does show some disorder, the relatively high temperature in which the samples become insulating suggests that Anderson localization is unlikely the central reason for the insulating state (53-55). Additional fitting was done on the basis of the variable range hopping equation as an attempt to determine whether Anderson localization is the root cause of the insulating state (56). We plotted  $\ln(\rho)$  versus  $T^{-1/(\nu+1)}$ , where  $\nu$  describes the hopping dimensionality, which can be equal to 1 (1D), 2 (2D), or 3 (3D) (55, 56). Anderson localization would typically result in an exponent of  $\nu = 3$  (55). We receive equally good fits to both  $\nu = 1$  and  $\nu = 2$  and less good fits to  $\nu = 3$ . This would suggest Efros-Shklovskii hopping mechanism (Coulombic repulsion) rather than Anderson localization for  $\nu = 1$ , although it should be noted that for electronically 2D samples, an exponent of  $\nu = 2$  could also suggest Anderson localization. Still, the lack of a clear best fit renders the data inconclusive. Alternatively, the system could form lattice or magnetic polarons. Here, the carriers would be localized around lattice distortions or local magnetic clouds (57). Again, the lack of magnetoresistance argues against magnetic polarons. Furthermore, the activation energy determined by transport (140 meV) is far higher than the energy of the optical modes we detect via Raman spectroscopy (~35→ 50 meV). Thus, our results point to a unusual hidden-order insulator resulting from doping into the flat bands of this kagome system. Hence, a number of additional experiments are called for, including spectroscopic (tunneling and photoemission) studies to uncover the detailed low-energy band structure. In addition, thermal, nonlinear optics or capacitance measurements of exfoliated materials may

prove fruitful in further exploring the unique correlated state of CsNi<sub>3</sub>S<sub>4</sub> (58, 59).

We showed here that soft chemistry can be used to introduce novel kagome materials that are not accessible via typical solid-state reactions. This enables the exploration of metastable compounds with exotic properties, such as flat bands at the Fermi level. Our method can, in principle, be extended to the related  $A_2TM_3Ch_4$  (A = K, Cs, Rb, TM = Ni, Pd Ch = S, Se) phases that have been reported to exist (60). Other exotic physical properties could thus be similarly accessed. For example, Rb<sub>2</sub>Pd<sub>3</sub>Se<sub>4</sub> has been shown to exhibit pressure-induced superconductivity (61). Further studies might also introduce the possibility of removing more Cs from Cs<sub>2</sub>Ni<sub>3</sub>S<sub>4</sub> samples to potentially reach kagome Ni<sub>3</sub>S<sub>4</sub>. Neilson et al. (62) have accessed a previously unreported binary nickel sulfide (Ni<sub>2</sub>S) through topochemical deintercalation of potassium in ternary K-Ni-S compounds. Similarly, other studies have reported oxidative deintercalation of alkali atoms from other alkali nickel chalcogenide compounds (63). Initial tests, however, in which the duration of acid treatment was increased were thus far not successful and resulted in CsNi<sub>3</sub>S<sub>4</sub>. Treatment with nitric, sulfuric, and acetic acid yielded the same result. Exploring other oxidizing agents, such as  $[Cu^{2+} + 2I^{-}]$  used in Neilson et al. (62), might be an avenue that warrants further exploration. In addition, further alteration of CsNi<sub>3</sub>S<sub>4</sub> by ion or molecule intercalation could lead to alternative electronic properties of interest. Intercalation chemistry in layered compounds can often lead to exotic electronic phenomena, such as the superconductivity produced in Li/ethylenediamene co-intercalated WTe2 (64). Co-intercalation with molecules could also be a tool to further separate the layers and avoiding band broadening due to layer interactions. Overall, this unreported, air-stable, layered kagome compound could provide an interesting scaffolding for various intercalants in future studies. In general, our methods open a door for exploring and manipulating kagome compounds and enable further study of their flat bands.

# **MATERIALS AND METHODS**

# Cs<sub>2</sub>Ni<sub>3</sub>S<sub>4</sub> synthesis

Cesium carbonate (99%; Sigma-Aldrich), nickel powder (99.7%; Sigma-Aldrich), and sulfur powder (99.5%; Alfa Aesar) were ground together in a mortar and pestle in a 6:1:12 molar ratio of Cs/Ni/S. The ground powders were pressed into a pellet and placed in an alumina crucible. The precursors were heated over 6 hours to 800°C in a flow furnace flowing argon. They were held at this temperature for 6 hours and then cooled to room temperature over 6 hours. The resulting product was then quickly washed with water and ethanol to remove extraneous sulfur compound impurities, followed by storage in an argon glovebox.

## CsNi<sub>3</sub>S<sub>4</sub> synthesis

CsNi<sub>3</sub>S<sub>4</sub> crystals were placed in a 0.1 M HCl (Sigma-Aldrich, ACS grade) solution in Milli-Q water under atmosphere. Once crystals stopped producing bubbles, they were washed with Milli-Q water and vacuum filtered.

# **Gas chromatography**

A 2 mg of Cs  $_{2-x}$ Ni $_3$ S $_4$  crystals was placed in a sealed vial containing argon. 2 ml of 0.1 M HCl was added to the vial via a syringe. After 1 min of bubbling, a 50  $\mu$ l of air sample was taken from the headspace and injected into an SRI 8610C gas chromatograph for a 10-min isotherm at

80° with He flow. This instrument used a Hayesep D packed column and thermal conductivity detector.

## X-ray photoelectron spectroscopy

XPS measurements were conducted on a Thermo Fisher K-Alpha with x-ray photoelectron spectrometer (XPS/ultraviolet photoelectron spectrometer). The parent compound was transported using a XPS vacuum module to prevent further oxidation. Both compounds were etched on "low" using a monoatomic argon ion beam at 2000-eV energy for 10 s per level. Data shown in this manuscript were etched four times and contained little to no hydrocarbon signal.

#### **DFT calculations**

Band structures were calculated with the VASP to perform the ab initio computations, where we use GGA of PBE exchange-correlation potential (37, 65–69). An energy cutoff of 400 eV is used. For simplicity, SOC is not included if not stated, as bands near the Fermi level are mainly from Ni and S, which have negligible SOC. The maximally localized Wannier functions are obtained using WANNIER90 (70–73), Wannhr\_symm in WannierTools (70–74). The minimal TB model is built with the help of MagneticTB (75).

Calculations on  $Cs_2Ni_3S_4$  performed on experimental geometry reported in the Inorganic Crystal Structure Database, without additional relaxation (76). The calculations on conventional unit cells used the meta-GGA the SCAN functional, recommended projector augmented wave potentials for all atoms, and an energy cutoff of 520 eV (47, 77, 78). We used the reported experimental geometry for  $Cs_2Ni_3S_4$  (79). The experimental structure of  $CsNi_3S_4$  was optimized before running electronic structure calculations. The experimental structure of  $CsNi_3S_4$  was optimized using the conjugate gradient algorithm implemented in VASP with the 0.25 trail step length (80). To model magnetism in  $CsNi_3S_4$ , we ran collinear and noncollinear spin-polarized calculations starting from different magnetic configurations. The magnetic configurations were calculated using the SCAN functional for increased accuracy (44).

## Magnetic characterization

All dc magnetic measurements were taken on a SQUID-VSM magnetic property measurement system 3 (Quantum Design). All measurements were taken using a straw holder. Air-sensitive samples were prepped by sealing them in parafilm first before attaching them to the holder. All measurements were background subtracted.

#### Charge transport

Resistivity ( $\rho$ ) was measured on single crystals with a length of 2.02 mm, a thickness of 0.028 mm and a distance between probes of 1.34 mm for Cs  $_{2-x}$ Ni $_3$ S4 and a length of 1.07 mm, and a thickness of 0.027 mm and a distance between probes of 0.373 mm for CsNi $_3$ S4 using a Quantum Design DynaCool PPMS from 50 to 300 K. Measurements were taken by attaching Au wires with silver paste (Dupont 4929 N) in a four-point collinear geometry with current along the ab plane. An additional transport measurement was conducted for CsNi $_3$ S4 with gold contacts to test the effects of direct silver paste contact on the data. A 5-nm layer of Ti was sputtered on the sample with 50-nm gold for the electrodes. Silver wires were attached to the gold contacts using silver paste. This method prevents direct contact of the sample surface with the silver paste, similar to the methods used in Hondou et al. (45) for Rb2Ni $_3$ S4. The resulting data show little change in the transport properties. Therefore, it is unlikely that the silver paste is affecting the accuracy of the data.

#### **Heat capacity**

Heat capacity was taken on a Quantum Design DynaCool PPMS with Apiezon N grease adhering the samples to the stage. Measurements were made on pressed pellets. Cs  $_{2-x}Ni_3S_4$  pellets were annealed overnight at 300°C overnight for structural integrity.

#### Powder x-ray diffraction

Phase purity and crystal quality of all samples were checked using PXRD patterns obtained from a STOE STADI P powder diffractometer with Mo-K $\alpha_1$  radiation and a Dectris Mythen 2R 1 K detector in the 2 $\theta$  range from 1° to 45°. Powder samples were run in 0.5-mm glass capillaries. The resulting pattern from each sample was refined using TOPAS V7 (Bruker AXS). Pattern for  $Cs_2Ni_3S_4$  was obtained from the ICSD (collection code: 627055).

#### **Electron diffraction**

Selected-area electron diffraction patterns for  $CsNi_3S_4$  were obtained on a Talos F200X scanning/transmission electron microscope (S/TEM) using a double-tilt holder. Distances for experimental patterns were measured in ImageJ. CrystalMaker software SingleCrystal was used to simulate the diffraction pattern based on the proposed structure. Distances for the simulated diffraction pattern were obtained in the Single-Crystal software.

#### Scanning/transmission electron microscopy (S/TEM)

The lamella sample for cross-sectional S/TEM studies was extracted from a bulk single crystal using a Helios DualBeam focused ion beam (FIB)/SEM system. The extraction process involved cutting out a portion of the crystal, followed by thinning it down to a thickness of approximately 50 nm. To minimize surface damage, the TEM lamella samples were subjected to a polishing step using a 2-kV gallium ion beam. Once the TEM lamella was obtained, it was carefully transferred to a Mo TEM grid and promptly loaded into the high S/TEM vacuum chamber to minimize oxygen and moisture attacking under ambient conditions.

HRSTEM images were taken on the Titan Cubed Themis 300 double Cs-corrected S/TEM. Distances on images were measured using ImageJ.

#### Raman

Raman spectroscopy data was collected on a pressed CsNi $_3$ S $_4$  pellet and CsNi $_3$ S $_4$  and parent compound crystals. The Raman spectroscopy measurements were performed with a custom-built low-temperature Raman spectroscopy setup in the backscattering configuration. The sample was excited with a 532-nm laser focused on the sample surface using  $100\times$  objective, and laser power was kept low ( $\le 0.1~\mu$ W) to avoid any local heating. The spectra were collected using an Andor spectrometer equipped with 1200 grooves/mm grating coupled with an Andor charge-coupled device detector, providing a resolution of approximately 1 cm  $^{-1}$ . Temperature-dependent measurements were performed with a closed cycle He-flow cryostat (Montana Instruments) under high vacuum  $1.0\times 10^{-7}$  Torr.

#### **FTIR**

FTIR data was collected using a Bruker Vertex 70 V Spectrometer system in a reflectance configuration. Measurements were done at room temperature over a range of 100 to 1800 meV on bulk crystal samples with  $15\times$  and  $40\times$  objectives.

#### **Supplementary Materials**

This PDF file includes:

Figs. S1 to S26 Tables S1 and S2 References

#### REFERENCES AND NOTES

- 1. B. Keimer, J. Moore, The physics of quantum materials. Nat. Phys. 13, 1045-1055 (2017).
- E. Dagotto, Complexity in strongly correlated electronic systems. Science 309, 257–262 (2005)
- V. I. Anisimov, F. Aryasetiawan, A. I. Lichtenstein, First-principles calculations of the electronic structure and spectra of strongly correlated systems: The LDA+ *U* method. *J. Phys. Condens. Matter* 9, 767 (1997).
- M. Jovanovic, L. M. Schoop, Simple chemical rules for predicting band structures of kagome materials. J. Am. Chem. Soc. 144, 10978–10991 (2022).
- L. Balents, C. R. Dean, D. K. Efetov, A. F. Young, Superconductivity and strong correlations in moiré flat bands. *Nat. Phys.* 16, 725–733 (2020).
- C. S. Chiu, D.-S. Ma, Z.-D. Song, B. A. Bernevig, A. A. Houck, Fragile topology in line-graph lattices with two, three, or four gapped flat bands. *Phys. Rev. Res.* 2, 043414 (2020).
- N. Regnault, Y. Xu, M.-R. Li, D.-S. Ma, M. Jovanovic, A. Yazdani, S. S. Parkin, C. Felser, L. M. Schoop, N. P. Ong, R. J. Cava, L. Elcoro, Z. Song, B. A. Bernevig, Catalogue of flat-band stoichiometric materials. *Nature* 603. 824–828 (2022).
- B. R. Ortiz, S. M. Teicher, Y. Hu, J. L. Zuo, P. M. Sarte, E. C. Schueller, A. M. Abeykoon, M. J. Krogstad, S. Rosenkranz, R. Osborn, R. Seshadri, L. Balents, J. He, S. D. Wilson, CsV<sub>3</sub>Sb<sub>5</sub>: A Z<sub>2</sub> topological kagome metal with a superconducting ground state. *Phys. Rev. Lett.* 125, 247002 (2020).
- Y. Hu, S. M. Teicher, B. R. Ortiz, Y. Luo, S. Peng, L. Huai, J. Ma, N. C. Plumb, S. D. Wilson, J. He, M. Shi, Topological surface states and flat bands in the kagome superconductor CsV<sub>3</sub>Sb<sub>5</sub>. Sci. Bull. 67, 495–500 (2022).
- M. Kang, L. Ye, S. Fang, J.-S. You, A. Levitan, M. Han, J. I. Facio, C. Jozwiak, A. Bostwick, E. Rotenberg, M. K. Chan, R. D. McDonald, D. Graf, K. Kaznatcheev, E. Vescovo, D. C. Bell, E. Kaxiras, J. Brink, M. Richter, M. P. Ghimire, J. G. Checkelsky, R. Comin, Dirac fermions and flat bands in the ideal kagome metal FeSn. *Nat. Mater.* 19, 163–169 (2020).
- M. L. Kiesel, R. Thomale, Sublattice interference in the kagome Hubbard model. Phys. Rev. B 86, 121105 (2012).
- 12. H. Hu, Q. Si, Coupled topological flat and wide bands: Quasiparticle formation and destruction. *Sci. Adv.* **9**, eadq0028 (2023).
- A. Korshunov, H. Hu, D. Subires, Y. Jiang, D. Călugăru, X. Feng, A. Rajapitamahuni, C. Yi,
   Roychowdhury, M. G. Vergniory, J. Strempfer, C. Shekhar, E. Vescovo, D. Chernyshov,
   A. H. Said, A. Bosak, C. Felser, B. A. Bernevig, S. Blanco-Canosa, Softening of a flat phonon mode in the kagome ScV<sub>6</sub>Sn<sub>6</sub>. arXiv:2304.09173 [cond-mat.str-el] (2023).
- Y. Jiang, H. Hu, D. Călugăru, C. Felser, S. Blanco-Canosa, H. Weng, Y. Xu, B. A. Bernevig, Kagome Materials II: SG 191: FeGe as a LEGO building block for the entire 1:6:6 series: Hidden d-orbital decoupling of flat band sectors, effective models and interaction Hamiltonians. arXiv:2311.09290 [cond-mat.str-el] (2023).
- J. Provost, G. Vallee, Riemannian structure on manifolds of quantum states. Commun. Math. Phys. 76, 289–301 (1980).
- R. Resta, The insulating state of matter: a geometrical theory. Euro. Phys. J. B 79, 121–137 (2011).
- 17. P. Törmä, Essay: Where can quantum geometry lead us? *Phys. Rev. Lett.* **131**, 240001 (2023).
- I. Komissarov, T. Holder, R. Queiroz, The quantum geometric origin of capacitance in insulators.. Nat. Commun. 15, 4621 – (2024).
- Y. Xu, L. Elcoro, G. Li, Z. Song, N. Regnault, Q. Yang, Y. Sun, S. Parkin, C. Felser,
   B. A. Bernevig, Three-dimensional real space invariants, obstructed atomic insulators and a new principle for active catalytic sites. arXiv:2111.02433 [cond-mat.mtrl-sci] (2021).
- Y. Xu, L. Elcoro, Z. Song, M. G. Vergniory, C. Felser, S. S. P. Parkin, N. Regnault, J. L. Mañes, B. A. Bernevig, Filling-enforced obstructed atomic insulators. *Phys. Rev. B* 109, 165139 (2024).
- P.Törmä, S. Peotta, B. A. Bernevig, Superconductivity, superfluidity and quantum geometry in twisted multilayer systems. *Nat. Rev. Phys.* 4, 528–542 (2022).
- J. Herzog-Arbeitman, V. Peri, F. Schindler, S. D. Huber, B. A. Bernevig, Superfluid weight bounds from symmetry and quantum geometry in flat bands. *Phys. Rev. Lett.* 128, 087002 (2022).
- J. Yu, C. J. Ciccarino, R. Bianco, I. Errea, P. Narang, B. A. Bernevig, Non-trivial quantum geometry and the strength of electron–phonon coupling. Nat. Phys. 20, 1262–1268 (2024).
- M. Kang, M. S. Fang, J. Yoo, B. R. Ortiz, Y. M. Oey, J. Choi, S. H. Ryu, J. Kim, C. Jozwiak,
   A. Bostwick, E. Rotenberg, E. Kaxiras, J. G. Checkelsky, S. D. Wilson, J.-H. Park, R. Comin,
   Charge order landscape and competition with superconductivity in kagome metals. *Nat. Mater.* 22, 186–193 (2023).
- M. Kang, S. Fang, L. Ye, H. C. Po, J. Denlinger, C. Jozwiak, A. Bostwick, E. Rotenberg, E. Kaxiras, J. G. Checkelsky, R. Comin, Topological flat bands in frustrated kagome lattice CoSn. *Nat. Commun.* 11, 4004 (2020).

# SCIENCE ADVANCES | RESEARCH ARTICLE

- L. Ye, M. Kang, J. Liu, F. Von Cube, C. R. Wicker, T. Suzuki, C. Jozwiak, A. Bostwick, E. Rotenberg, D. C. Bell, L. Fu, R. Comin, J. G. Checkelsky, Massive Dirac fermions in a ferromagnetic kagome metal. *Nature* 555, 638–642 (2018).
- M. Han, H. Inoue, S. Fang, C. John, L. Ye, M. K. Chan, D. Graf, T. Suzuki, M. P. Ghimire, W. J. Cho, E. Kaxiras, J. G. Checkelsky, Evidence of two-dimensional flat band at the surface of antiferromagnetic kagome metal FeSn. *Nat. Commun.* 12, 5345 (2021).
- D. Kim, F. Liu, Realization of flat bands by lattice intercalation in kagome metals. Phys. Rev. B 107, 205130 (2023).
- D. Guterding, H. O. Jeschke, R. Valentí, Prospect of quantum anomalous Hall and quantum spin Hall effect in doped kagome lattice Mott insulators. Sci. Rep. 6, 25988 (2016).
- 30. I. Mazin, H. O. Jeschke, F. Lechermann, H. Lee, M. Fink, R. Thomale, R. Valentí, Theoretical prediction of a strongly correlated Dirac metal. *Nat. Commun.* **5**, 4261 (2014).
- Y. Liu, Y. Wang, Y. Cai, Z. Hao, X.-M. Ma, L. Wang, C. Liu, J. Chen, L. Zhou, J. Wang, S. Wang, H. He, Y. Liu, S. Cui, B. Huang, J. Wang, C. Chen, J. W. Mei, Doping evolution of superconductivity, charge order, and band topology in hole-doped topological kagome superconductors Cs(V1–xTix)3Sb5. *Phys. Rev. Mater.* 6, 064801 (2014).
- Y. M. Oey, F. Kaboudvand, B. R. Ortiz, R. Seshadri, S. D. Wilson, Tuning charge density wave order and superconductivity in the kagome metals KV<sub>3</sub>Sb<sub>5-x</sub>Sn<sub>x</sub> and RbV<sub>3</sub>Sb<sub>5-x</sub>Sn<sub>x</sub>. Phys. Rev. Mater. 6, 074802 (2022).
- D. E. Freedman, W. H. Harman, D. Harris, G. J. Long, C. J. Chang, J. R. Long, Site specific X-ray anomalous dispersion of the geometrically frustrated kagomé magnet, herbertsmithite, ZnCu<sub>3</sub>(OH)<sub>6</sub>Cl<sub>2</sub>. J. Am. Chem. Soc. 132, 16185–16190 (2010).
- Z. Kelly, M. Gallagher, T. McQueen, Electron doping a kagome spin liquid. Phys. Rev. X 6, 041007 (2016).
- Q. Liu, Q. Yao, Z. A. Kelly, C. M. Pasco, T. M. McQueen, S. Lany, A. Zunger, Electron doping of proposed kagome quantum spin liquid produces localized states in the band gap. *Phys. Rev. Lett.* 121, 186402 (2018).
- W. Bronger, R. Rennau, D. Schmitz, Die Kristallstrukturen von Cs₂Ni₃S₄. Zeitschrift für Kristallographie Crystalline Mater. 183, 201–206 (1988).
- J. P. Perdew, K. Burke, M. Ernzerhof, Generalized gradient approximation made simple. Phys. Rev. Lett. 77, 3865–3868 (1996).
- B. L. Hoff, G. Cheng, G. Villalpando, F. Yuan, N. Yao, L. M. Schoop, Chemically exfoliated nanosheets of β-Bi<sub>2</sub>O<sub>3</sub>. J. Phys Mater 5, 044004 (2022).
- V. Gvozdetskyi, K. Rana, R. A. Ribeiro, A. Mantravadi, A. N. Adeyemi, R. Wang, H. Dong, K.-M. Ho, Y. Furukawa, P. C. Canfield, J. V. Zaikina, From layered antiferromagnet to 3D ferromagnet: LiMnBi-to-MnBi magneto-structural transformation. *Chem. Mater.* 35, 3236–3248 (2023).
- G. M. Friederichs, I. Schellenberg, R. Pöttgen, V. Duppel, L. Kienle, J. S. auf der Günne,
   D. Johrendt, Metastable 11 K Superconductor Na<sub>1-y</sub>Fe<sub>2-x</sub>As<sub>2</sub>. *Inorg. Chem.* 51, 8161–8167 (2012).
- 41. G. Villalpando, A. M. Ferrenti, R. Singha, X. Song, G. Cheng, N. Yao, L. M. Schoop, Chemical exfoliation toward magnetic 2D VOCI monolayers. *ACS Nano* 16, 13814–13820 (2022).
- X. Zhou, B. Wilfong, H. Vivanco, J. Paglione, C. M. Brown, E. E. Rodriguez, Metastable layered cobalt chalcogenides from topochemical deintercalation. J. Am. Chem. Soc. 138, 16432–16442 (2016).
- X. Song, S. N. Schneider, G. Cheng, J. F. Khoury, M. Jovanovic, N. Yao, L. M. Schoop, Kinetics and evolution of magnetism in soft-chemical synthesis of CrSe<sub>2</sub> from KCrSe<sub>2</sub>. Chem. Mater. 33, 8070–8078 (2021).
- J. Sun, A. Ruzsinszky, J. P. Perdew, Strongly constrained and appropriately normed semilocal density functional. *Phys. Rev. Lett.* 115, 036402 (2015).
- K. Hondou, Y. Fujiwara, T. Kato, K. Iio, A. Saiki, M. Usuda, N. Hamada, Reinvestigation of magnetism and electric transport in a ternary transition metal chalcogenide Rb<sub>2</sub>Ni<sub>3</sub>S<sub>4</sub>. J. Alloys Comp. 333, 274–281 (2002).
- 46. K. Hondou, M. Usuda, K. Iio, Water-induced and Co-filling control induced ferromagnetism in  $Rb_2Ni_3S_4$ . Ceramics Silikáty **49**, 1–6 (2005).
- D.-Y. Noh, J.-H. Choy, Magnetic properties of nickel(III) bis(benzene-1,2-dithiolate); (n-Bu<sub>4</sub>N) [Ni(dmbit)<sub>2</sub>] and (n-Bu<sub>4</sub>N) [Ni(dmbbip)<sub>2</sub>]. Synth. Met. 70, 1059–1060 (1995).
- P. A. Beck, H. Claus, Density of states information from low temperature specific heat measurements. J. Res. Natl. Bur. Stand A Phys. Chem. 74A, 449–454 (1970).
- L. Ye, S. Fang, M. G. Kang, J. Kaufmann, Y. Lee, J. Denlinger, C. Jozwiak, A. Bostwick, E. Rotenberg, E. Kaxiras, D. C. Bell, O. Janson, R. Comin, J. G. Checkelsky, A flat band-induced correlated kagome metal. arXiv:2106.10824 [cond-mat.mtrl-sci] (2021).
- S. Kondo, D. Johnston, C. Swenson, F. Borsa, A. Mahajan, L. Miller, T. Gu, A. Goldman, M. Maple, D. Gajewski, E. J. Freeman, N. R. Dilley, R. P. Dickey, J. Merrin, K. Kojima, G. M. Luke, Y. J. Uemura, O. Chmaissem, J. D. Jorgensen, LiV<sub>2</sub>O<sub>4</sub>: A heavy fermion transition metal oxide. *Phys. Rev. Lett.* **78**, 3729 (1997).
- K. Miyoshi, E. Morikuni, K. Fujiwara, J. Takeuchi, T. Hamasaki, Mass-enhanced Fermi-liquid ground state in Na<sub>1.5</sub>Co<sub>2</sub>O<sub>4</sub>. Phys. Rev. B 69, 132412 (2004).
- S. Burch, A. Schafgans, N. Butch, T. Sayles, M. Maple, B. C. Sales, D. Mandrus, D. Basov, Optical study of interactions in a d-electron Kondo lattice with ferromagnetism. *Phys. Rev. Lett.* 95, 046401 (2005).
- S. Lei, S. M. L. Teicher, A. Topp, K. Cai, J. Lin, G. Cheng, T. H. Salters, F. Rodolakis,
   J. L. McChesney, S. Lapidus, N. Yao, M. Krivenkov, D. Marchenko, A. Varykhalov, C. R. Ast,

- R. Car, J. Cano, M. G. Vergniory, N. P. Ong, L. M. Schoop, Band engineering of dirac semimetals using charge density waves. *Adv. Mater.* **33**, 2101591 (2021).
- E. Díaz, G. Herrera, S. Oyarzún, R. C. Munoz, Evidence of weak Anderson localization revealed by the resistivity, transverse magnetoresistance and Hall effect measured on thin Cu films deposited on mica. Sci. Rep. 11, 17820 (2021).
- T. Ying, Y. Gu, X. Chen, X. Wang, S. Jin, L. Zhao, W. Zhang, X. Chen, Anderson localization of electrons in single crystals: Li<sub>x</sub>Fe<sub>2</sub>Se<sub>8</sub>. Sci. Adv. 2, e1501283 (2016).
- X. Chen, L. Bauernfeind, H. Braun, Na<sub>0.5</sub>La<sub>0.5</sub>RuO<sub>3</sub>: Structure and electronic properties. *Phys. Rev. B* 55, 6888–6895 (1997).
- M. B. Salamon, M. Jaime, The physics of manganites: Structure and transport. Rev. Modern Phys. 73, 583–628 (2001).
- Q. Ma, A. G. Grushin, K. S. Burch, Topology and geometry under the nonlinear electromagnetic spotlight. *Nat. Mater.* 20, 1601–1614 (2021).
- B. Hunt, J. D. Sanches-Yamagishi, A. F. Young, M. Yankowitz, B. J. Leroy, K. Watanabe, T. Taniguchi, P. Moon, M. Koshino, P. Jarillo-Herrero, R. C. Ashoori, Massive dirac fermions and hofstadter butterfly in a van der Waals heterostructure. *Science* 340, 1427–1430 (2013).
- W. Bronger, J. Eyck, W. Rüdorff, A. Stöussel, Über Thio- und Selenoniccolate und -palladate der schweren Alkalimetalle. Zeitschrift für anorganische und allgemeine Chemie 375, 1–7 (1970).
- Q. Li, Y. Wu, X. Fan, Y.-J. Zhang, X. Zhu, Z. Zhu, Y. Li, H.-H. Wen, Superconductivity arising from pressure-induced emergence of a Fermi surface in the kagome-lattice chalcogenide 4. Phys. Rev. B 106, 214501 (2022).
- J. R. Neilson, T. M. McQueen, Bonding, ion mobility, and rate-limiting steps in deintercalation reactions with ThCr<sub>2</sub>Si<sub>2</sub>-type KNi<sub>2</sub>Se<sub>2</sub>. J. Am. Chem. Soc. 134, 7750–7757 (2012).
- X. Zhou, D. J. Mandia, H. Park, M. Balasubramanian, L. Yu, J. Wen, A. Yakovenko,
   D. Y. Chung, M. G. Kanatzidis, New compounds and phase selection of nickel sulfides via oxidation state control in molten hydroxides. J. Am. Chem. Soc. 143, 13646–13654 (2021).
- 64. M. Ono, T. Noji, M. Harada, K. Sato, T. Kawamata, M. Kato, New lithium- and ethylenediamine-intercalated superconductors Lix(C<sub>2</sub>H<sub>8</sub>N<sub>2</sub>)<sub>y</sub>WTe<sub>2</sub>. *J. Physical Soc. Japan* **90**. 014706 (2021).
- G. Kresse, J. Furthmüller, Efficiency of ab-initio total energy calculations for metals and semiconductors using a plane-wave basis set. Computat. Mater. Sci. 6, 15–50 (1996).
- G. Kresse, J. Hafner, Ab initiomolecular dynamics for open-shell transition metals. *Phys. Rev. B* 48, 13115–13118 (1993).
- G. Kresse, J. Hafner, Ab initio molecular dynamics for liquid metals. *Phys. Rev. B* 47, 558–561 (1993).
- G. Kresse, J. Hafner, Ab initiomolecular-dynamics simulation of the liquid-metalamorphous-semiconductor transition in germanium. *Phys. Rev. B* 49, 14251–14269 (1994).
- G. Kresse, J. Furthmüller, Efficient iterative schemes for ab initio total-energy calculations using a plane-wave basis set. *Phys. Rev. B* 54, 11169–11186 (1996).
- N. Marzari, D. Vanderbilt, Maximally localized generalized Wannier functions for composite energy bands. Phys. Rev. B 56, 12847–12865 (1997).
- I. Souza, N. Marzari, D. Vanderbilt, Maximally localized Wannier functions for entangled energy bands. *Phys Rev. B* 65, 035109 (2001).
- N. Marzari, A. A. Mostofi, J. R. Yates, I. Souza, D. Vanderbilt, Maximally localized Wannier functions: Theory and applications. Rev. Mod. Phys. 84, 1419–1475 (2012).
- G. Pizzi, V. Vitale, R. Arita, S. Blüge, F. Freimuth, G. Géranton, M. Gibertini, D. Gresch, C. Johnson, T. Koretsune, J. Ibañez-Azpiroz, H. Lee, J. M. Lihm, D. Marchand, A. Marrazzo, Y. Mokrousov, J. I. Mustafa, Y. Nohara, Y. Nomura, L. Paulatto, S. Poncé, T. Ponweiser, J. Qiao, F. Thöle, S. S. Tsirkin, M. Wierzbowska, N. Marzari, D. Vanderbilt, I. Souza, A. A. Mostofi, J. R. Yates, Wannier90 as a community code: New features and applications. J. Phys. Condens. Matter 32, 165902 (2020).
- Q.Wu, S. Zhang, H.-F. Song, M. Troyer, A. A. Soluyanov, WannierTools: An open-source software package for novel topological materials. Comput. Phys. Commun. 224, 405–416 (2018).
- Z. Zhang, Z.-M. Yu, G.-B. Liu, Y. Yao, MagneticTB: A package for tight-binding model of magnetic and non-magnetic materials. Comput. Phys. Commun. 270, 108153 (2022).
- W. Bronger, R. Rennau, D. Schmitz, Schichtstrukturen ternärer Chalkogenide A<sub>2</sub>M<sub>3</sub>X<sub>4</sub>
   (A ≜ K, Rb, Cs; M ≜ Ni, Pd, Pt; X ≜ S, Se). J. Inorganic Gen. Chem. 597, 27–32 (1991).
- 77. P. E. Blöchl, Projector augmented-wave method. Phys. Rev. B 50, 17953–17979 (1994).
- G. Kresse, D. Joubert, From ultrasoft pseudopotentials to the projector augmented-wave method. *Phys. Rev. B* 59, 1758–1775 (1999).
- W. Bronger, R. Rennau, D. Schmitz, Schichtstrukturen ternrer Chalkogenide A2M3X4 (A? K, Rb, Cs; M? Ni, Pd, Pt; X? S, Se). Zeitschrift für anorganische und allgemeine Chemie 597, 27–32 (1991).
- W. H. Press, S. Teukolsky, W. T. Vetterling, B. Flannery, Numerical recipes in C. (Cambridge Univ. Press, 1992).
- W. Brinkman, R. J. Elliot, Theory of spin-space groups. Proc. R. Soc. A Math. Phys. Sci. 294, 343–358 (1966).
- 82. D. Litvin, W. Opechowski, Spin groups. *Physica* **76**, 538–554 (1974).
- J. Yang, Z.-X. Liu, C. Fang, Symmetry invariants and classes of quasi-particles in magnetically ordered systems having weak spin-orbit coupling. arXiv:2105.12738 [cond-mat.mes-hall] (2021).

# SCIENCE ADVANCES | RESEARCH ARTICLE

- Y. Jiang, Z. Song, T. Zhu, Z. Fang, H. Weng, Z.-X.Liu, J. Yang, C. Fang, Enumeration of spin-space groups: Towards a complete description of symmetries of magnetic orders. arXiv: 2307.10371 (2023).
- Z. Xiao, J. Zhao, Y. Li, R. Shindou, Z.-D. Song, Spin space groups: Full classification and applications. arXiv:2307.10364 [cond-mat.mes-hall] (2023).
- J. Ren, X. Chen, Y. Zhu, Y. Yu, A. Zhang, J. Li, C. Li, Q. Liu, Enumeration and representation of spin space group. arXiv:2307.10369 [Preprint] (2023).

Acknowledgment: We acknowledge the assistance of F. Katmer in the theoretical calculations. We would also like to acknowledge the assistance of X. Yang, Z. Zhu, and P. Ong for gold coating transport samples. Funding: This research was primarily supported by the DOD's office of naval research (ONR) (award number N00014-21-1-2733), the Princeton Center for Complex Materials, a National Science Foundation (NSF)-MRSEC program (DMR-2011750), and the Gordon and Betty Moore Foundation'S EPIOS initiative (grant number GBMF9064). Additional support was provided by the Princeton Catalysis Initiative (PCI) and the Packard foundation, which funded equipment purchases. We acknowledge the use of Princeton's Imaging and Analysis Center, which is partially supported by the Princeton Center for Complex Materials, an NSF-MRSEC program (DMR-2011750). B.H. is supported by the NSF Graduate Research Fellowship Program under grant number DGE-2039656. J.F.K. would like to acknowledge support from the Arnold O. Beckman Postdoctoral Fellowship. V.M.P. acknowledges the primary support of the U.S. Department of Energy (DOE), Office of Science, Office of Basic Energy Sciences under award number DE-SC0018675. B.S. acknowledges support by the Air Force Office of Scientific Research under award number FA9550-20-1-0246. K.S.B. is grateful for the support of the Office of Naval Research under award number N00014-20-1-2308. B.A.B. was supported by the Gordon and Betty Moore Foundation through grant no.GBMF8685 toward the Princeton theory program, the Gordon and Betty Moore

Foundation's EPiQS Initiative (grant no. GBMF11070), Office of Naval Research (ONR grant no. N00014-20-1-2303), Global Collaborative Network Grant at Princeton University, BSF Israel US foundation no. 2018226, NSF-MERSEC (grant no. MERSEC DMR 2011750), the Simons theory collaboration on frontiers of superconductivity, and Simons collaboration on mathematical sciences. Author contributions: G.V., M.J., and L.M.S. founded the idea for this project. G.V. synthesized both the parent compound and the product. G.V. performed the XRD, SEM/EDX, and magnetic properties measurement system measurements, M.J. performed initial DFT calculations. Y.J. H.H. D.C. and B.A.B. performed the analysis of the flat bands, including tight binding models, symmetry analysis and calculations using a Hubbard U. B.H. performed the Rietveld refinements for the structure. G.V. and B.H. performed the selected-area electron diffraction and measured peak distances. R.S. and G.V. executed the magnetic and transport measurements. F.Y. carried out FIB and performed HRSTEM. J.F.K., R.S., and G.V. conducted the heat capacity measurements. N.M. and G.V. performed the exfoliation. S.D. performed the gas chromatography measurements, B.S. conducted Raman experiments, V.M.P. conducted the FTIR measurments. K.S.B. provided insight into the Raman and FTIR measurments. G.V. C.J.P., J.M.M., J.F.K., K.S.B., and R.S. provided important insight into the magnetic, transport, and heat capacity measurements. All data were analyzed by G.V. with L.M.S. supervising. G.V., M.J., B.H., and L.M.S. wrote the first draft of the manuscript. All authors provided discussion of results and scientific input to the manuscript. Competing interests: The authors declare that they have no competing interests. Data and materials availability: All data needed to evaluate the conclusions in the paper are present in the paper and/or the Supplementary Materials.

Submitted 28 September 2023 Accepted 15 August 2024 Published 20 September 2024 10.1126/sciadv.adl1103